Quaternary Science Reviews 78 (2013) 155–168

Contents lists available at ScienceDirect

Quaternary Science Reviews

journal homepage: www.elsevier.com/locate/quascirev

A Stalagmite record of Holocene Indonesian–Australian summer monsoon variability from the Australian tropics

Rhawn F. Denniston [a,*], Karl-Heinz Wyrwoll [b], Victor J. Polyak [c], Josephine R. Brown [d], Yemane Asmerom [c], Alan D. Wanamaker Jr. [e], Zachary LaPointe [c], Rebecca Ellerbroek [a], Michael Barthelmes [a], Daniel Cleary [a], John Cugley [f], David Woods [g], William F. Humphreys [b,h,i]

[a] Department of Geology, Cornell College, Mount Vernon, IA, USA
[b] University of Western Australia, Perth, Western Australia, Australia
[c] Department of Earth and Planetary Sciences, University of New Mexico, Albuquerque, NM, USA
[d] Centre for Australian Weather and Climate Research, Melbourne, Australia
[e] Department of Geological and Atmospheric Sciences, Iowa State University, Ames, IA, USA
[f] Kimberley Toad Busters, Kununurra, Western Australia, Australia
[g] Department of Environment and Conservation, Broome, Western Australia, Australia
[h] Western Australian Museum, Welshpool DC, Western Australia, Australia
[i] University of Adelaide, Adelaide, South Australia, Australia

ARTICLE INFO

Article history:
Received 22 April 2013
Received in revised form
7 August 2013
Accepted 8 August 2013
Available online

Keywords:
Stalagmite
Oxygen isotope
Indonesian–Australian summer monsoon
El Nino-Southern Oscillation
Intertropical convergence zone
Holocene

ABSTRACT

Oxygen isotopic data from a suite of calcite and aragonite stalagmites from cave KNI-51, located in the eastern Kimberley region of tropical Western Australia, represent the first absolute-dated, high-resolution speleothem record of the Holocene Indonesian–Australian summer monsoon (IASM) from the Australian tropics. Stalagmite oxygen isotopic values track monsoon intensity via amount effects in precipitation and reveal a dynamic Holocene IASM which strengthened in the early Holocene, decreased in strength by 4 ka, with a further decrease from ~2 to 1 ka, before strengthening again at 1 ka to years to levels similar to those between 4 and 2 ka. The relationships between the KNI-51 IASM reconstruction and those from published speleothem time series from Flores and Borneo, in combination with other data sets, appear largely inconsistent with changes in the position and/or organization of the Intertropical Convergence Zone (ITCZ). Instead, we argue that the El Niño/Southern Oscillation (ENSO) may have played a dominant role in driving IASM variability since at least the middle Holocene. Given the muted modern monsoon rainfall responses to most El Niño events in the Kimberley, an impact of ENSO on regional monsoon precipitation over northwestern Australia would suggest non-stationarity in the long-term relationship between ENSO forcing and IASM rainfall, possibly due to changes in the mean state of the tropical Pacific over the Holocene.

1. Introduction

The modern climate of the Australian tropics is dominated by the IASM, part of an extensive monsoon system ranging across the Maritime Continent and the Indo-Pacific Warm Pool (IPWP) and extending southwards into northern Australia (Fig. 1). The IASM serves as a major tropical heat source that plays a significant role in the planetary scale circulation and is strongly linked to its East Asian Summer Monsoon (EASM) counterpart (McBride, 1987; Neale and Slingo, 2003; Chang et al., 2004). Marine and continental paleoclimate studies have reconstructed the IASM at millennial scales during the Last Glacial, and produced a largely consistent pattern of IASM variability in which the IASM trough, which is tied to positioning of the ITCZ, was displaced latitudinally due to changes in North Atlantic climate and meridional ocean circulation (Partin et al., 2007; Griffiths et al., 2009; Lewis et al., 2010; Muller et al., 2012; Denniston et al., 2013) (Table 1).

For the Holocene, a more complex regional picture of monsoon events over the wider IASM and EASM regions has begun to emerge in which: (i) stalagmites from Dongge Cave, China (25°N, 108°E)

* Corresponding author.
E-mail address: rdenniston@cornellcollege.edu (R.F. Denniston).

0277-3791/$ – see front matter © 2013 Elsevier Ltd. All rights reserved.
http://dx.doi.org/10.1016/j.quascirev.2013.08.004

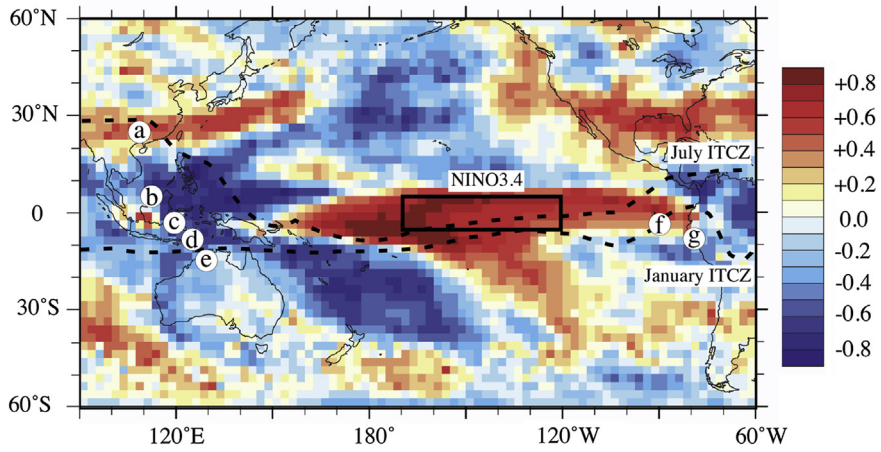

Fig. 1. Map of the Pacific Basin showing correlations between regional rainfall anomalies and NINO3.4 (box) SST for the years 1979–2008 based on the GPCP database. Stalagmite records of Holocene monsoon variability cited in text are: a. Dongge Cave (Wang et al., 2005); b. Gunung Buda, Borneo (Partin et al., 2007); c. Sulawasi (Tierney et al., 2012); d. Liang Luar, Flores (Griffiths et al., 2009); e. KNI-51 (this study); f. El Junco, Galapagos (Conroy et al., 2008); g. Laguna Pallcacocha, Ecuador (Moy et al., 2002).

record decreases in EASM strength during the Holocene in close agreement with reductions in precession-driven summer insolation in the Northern Hemisphere (Wang et al., 2005); (ii) stalagmites from Gunung Buda, Borneo (5°N, 114°E) reveal IASM strength that tracked differences in fall and spring insolation, with peak rainfall during the middle Holocene (Partin et al., 2007); (iii) stalagmites from Liang Luar, Flores (8°S, 120°E) record a middle Holocene characterized by a period of reduced rainfall, opposite in sign to the Borneo record, and attributed to regional SST variations associated with the Indian Ocean Dipole (IOD; Griffiths et al., 2010);

Table 1
U/Th Isotopic Ratios and ^{230}Th Ages of KNI-51 Stalagmites.

Sample	Mineral	Distance to base (mm)	^{238}U (ng/g)	^{232}Th (pg/g)	δ^{234}U[a] (corr'd)	Error[b]	^{230}Th/^{238}U (activity)	Error	^{230}Th/^{232}Th (ppm)	Error	Uncorrected Age (yr)	Error (yr)	Corrected[c] Age (yr)	Age[d] (yr BP)	Error (yr)
0	Calcite	192	422	15,569	409.7	2.0	0.014	0.00034	6.4	0.2	1109	27	345	285	764
0	Calcite	181	84	3988	450.3	5.0	0.065	0.00241	22.7	0.9	5006	191	4054	3994	972
0	Calcite	173	183	3261	444.2	2.0	0.061	0.00073	56.7	0.9	4752	58	4392	4332	365
0	Calcite	156	452	5793	424.3	1.3	0.067	0.00055	86.7	1.1	5297	45	5034	4974	266
0	Calcite	148	106	2196	460.0	2.4	0.070	0.00133	55.5	1.5	5360	105	4945	4885	428
0	Calcite	141	122	1113	446.0	2.6	0.070	0.00139	126.2	6.1	5426	111	5242	5182	215
0	Calcite	108	100	2518	474.8	1.9	0.079	0.00110	51.4	1.5	6003	86	5502	5442	508
0	Calcite	106	112	1207	480.4	1.8	0.079	0.00110	121.5	3.9	6021	86	5809	5749	229
0	Calcite	97	72	1427	441.5	2.2	0.080	0.00180	66.4	2.4	6250	144	5847	5787	427
0	Calcite	77	136	579	506.0	2.0	0.108	0.00076	418.3	15.4	8130	60	8048	7988	102
0	Calcite	64	82	2020	445.7	2.9	0.098	0.00220	65.5	2.5	7664	179	7167	7107	528
0	Calcite	54	84	429	457.5	2.4	0.114	0.00168	366.0	32.4	8889	138	8787	8727	172
0	Calcite	44	89	2222	458.3	2.3	0.111	0.00149	73.3	1.7	8663	122	8164	8104	514
0	Calcite	36	136	579	506.0	2.0	0.108	0.00076	418.3	15.4	8130	60	8048	7988	102
3	Aragonite	687	4494	17,629	994.6	2.0	0.056	0.00008	234.1	0.7	3095	5	3037	2977	29
3	Aragonite	245	6994	3166	938.6	1.9	0.056	0.00009	2049.4	41.2	3219	6	3212	3152	7
3	Aragonite	5	5411	3375	969.7	2.0	0.069	0.00010	1830.4	41.3	3914	7	3904	3844	8
4	Calcite	475	91	2717	461.6	1.6	0.106	0.00086	58.3	0.6	8233	70	7634	7574	602
4	Calcite	315	99	1041	453.5	2.3	0.102	0.00090	160.2	4.1	7934	74	7724	7664	222
4	Calcite	307	119	1589	492.9	1.7	0.106	0.00090	131.5	2.4	8079	72	7819	7759	269
4	Calcite	240	135	2104	506.4	1.3	0.113	0.00083	119.7	1.8	8566	66	8264	8204	309
4	Calcite	216	154	3979	488.5	1.4	0.115	0.00075	73.6	0.7	8821	60	8315	8255	509
7	Aragonite	1021	4434	1246	1345.0	1.4	0.049	0.00019	2851.9	65.0	2288	9	2285	2225	10
7	Aragonite	527	4376	1355	1337.3	1.6	0.059	0.00041	3139.8	134.6	2792	20	2789	2729	20
7	Aragonite	57	11,822	21,578	1302.6	1.5	0.066	0.00027	593.9	2.5	3167	13	3143	3083	27
10	Aragonite	617	2238	54,450	1654.6	1.8	0.017	0.00013	11.7	0.1	710	5	443	383	267
10	Aragonite	414	2651	27,445	1658.1	1.8	0.021	0.00012	33.9	0.2	877	5	763	703	113
10	Aragonite	357	2520	33,068	1616.1	2.7	0.028	0.00014	35.6	0.2	1187	6	1041	981	146
10	Aragonite	134	2213	27,637	1569.2	1.5	0.031	0.00022	40.8	0.3	1319	9	1177	1117	142
10	Aragonite	12	2488	122,539	1630.5	8.3	0.043	0.00017	14.3	0.1	1782	9	1236	1176	546
11	Aragonite	41	10,238	1488	1338.4	1.1	0.00003	0.00001	3.8	1.5	2	1	0	−60	2
11	Aragonite	30	6049	643	1380.3	1.0	0.001	0.00002	215.5	11.8	64	1	62	2	2
11	Aragonite	21	6382	579	1358.8	1.9	0.002	0.00003	446.8	32.1	114	1	113	53	2
11	Aragonite	9	4686	4432	1359.9	1.7	0.005	0.00004	82.4	1.0	219	2	207	147	12
11	Aragonite	4	5321	6216	1354.6	1.9	0.005	0.00005	72.2	0.8	237	2	223	163	15
A1	Aragonite	530	3688	26,213	1012.8	2.0	0.066	0.00014	153.8	0.8	3662	9	3559	3499	103
A1	Aragonite	304	8154	2875	900.8	1.9	0.062	0.00008	2894.1	93.4	3619	6	3613	3553	8
A1	Aragonite	24	4646	649	1098.0	2.1	0.070	0.00012	8282.9	801.9	3721	7	3719	3659	8
A2-side 1	Aragonite	17	12,576	10,201	943.8	2.0	0.083	0.00012	1689.1	7.0	4780	9	4768	4708	15
A2-side 1	Aragonite	2	7032	8832	995.2	2.0	0.086	0.00013	1132.1	11.0	4834	9	4816	4756	20

Table 1 (*continued*)

Sample	Mineral	Distance to base (mm)	^{238}U (ng/g)	^{232}Th (pg/g)	δ^{234}U[a] (corr'd)	Error[b]	^{230}Th/^{238}U (activity)	Error	^{230}Th/^{232}Th (ppm)	Error	Uncorrected Age (yr)	Error (yr)	Corrected[c] Age (yr)	Age[d] (yr BP)	Error (yr)
A2-side 2	Aragonite	12	4407	14,463	1124.2	2.1	0.088	0.00011	443.5	2.3	4645	8	4600	4540	46
A2-side 2	Aragonite	2	9559	4620	902.0	1.9	0.080	0.00010	2716.5	31.0	4678	8	4671	4611	11
A3	Calcite	870	3436	39,715	1087.2	2.2	0.102	0.00013	145.9	0.3	5498	9	5337	5277	161
A3	Aragonite	870	3065	11,024	1106.2	2.1	0.098	0.00013	451.9	2.1	5247	9	5198	5138	50
A3	Aragonite	670	7251	5568	1044.8	2.1	0.098	0.00014	2103.9	13.1	5376	9	5365	5305	14
A3	Aragonite	149	3468	11,262	1067.4	2.1	0.106	0.00016	538.8	3.7	5770	11	5724	5664	47
A3	Aragonite	130	5222	26,773	944.2	2.0	0.101	0.00021	324.5	2.6	5835	14	5758	5698	78
A3	Aragonite	62	17,643	10,487.9	1139.8	2.2	0.110	0.00014	3057.2	27.3	5792	10	5784	5724	13
B	Calcite	540	7642	9945	924.1	1.9	0.048	0.00007	603.3	1.9	2738	5	2718	2658	20
B	Aragonite	540	9072	1707	899.9	1.9	0.047	0.00007	4135.7	68.2	2748	5	2745	2685	6
B	Aragonite	640	5681	3898	897.6	1.9	0.046	0.00007	1098.4	9.1	2664	5	2653	2593	12
C	Aragonite	755	6904	7187	852.0	1.9	0.132	0.00015	2095.4	17.0	8125	13	8109	8049	21
C	Aragonite	465	5346	30,437	833.6	1.9	0.135	0.00015	391.9	0.8	8405	13	8315	8255	91
C	Aragonite	68	5153	24,552	812.6	1.9	0.142	0.00251	491.0	8.9	8941	164	8864	8804	181
F	Aragonite	609	8171	775	1330.4	2.3	0.008	0.00002	1438.1	55.0	388	1	387	327	1
F	Aragonite	398	5017	8300	1342.8	2.3	0.013	0.00004	126.9	0.7	594	2	574	514	21
F	Aragonite	307	5289	4522	1321.0	2.3	0.014	0.00003	270.0	2.4	660	2	649	589	11
F	Aragonite	189	5223	3019	1340.7	2.3	0.016	0.00003	453.9	4.8	744	2	737	677	7
F	Aragonite	124	6471	452	1341.3	2.3	0.017	0.00003	3964.5	257.7	786	2	785	725	2
F	Aragonite	20	6188	3555	1349.1	2.4	0.020	0.00004	570.7	8.1	928	2	920	860	7
G	Aragonite	632	6024	1393	1334.9	2.3	0.008	0.00003	573.9	15.0	377	2	374	314	3
G	Aragonite	575	11,955	2248	1176.8	2.2	0.008	0.00003	699.1	9.2	400	1	398	338	3
G	Aragonite	496	5886	604	1168.9	2.2	0.009	0.00003	1401.1	78.3	440	1	438	378	2
G	Aragonite	389	5613	921	1145.1	2.1	0.010	0.00002	979.9	31.2	497	1	495	435	3
G	Aragonite	222	4187	1482	1210.8	2.2	0.012	0.00004	537.4	12.1	571	2	566	506	5
G	Aragonite	108	3281	8510	1146.7	2.2	0.013	0.00003	82.3	0.2	660	2	625	565	35
G	Aragonite	5	4836	6182	1053.1	2.1	0.013	0.00004	170.9	1.1	706	2	688	628	18
H	Aragonite	234	7145	9500	1273.8	2.3	0.069	0.00010	853.6	0.8	3361	6	3344	3284	18
H	Aragonite	207	7324	3287	1282.9	2.3	0.070	0.00012	2585.9	4.7	3425	7	3419	3359	9
H	Aragonite	181	5262	6024	1272.2	2.3	0.070	0.00011	1015.6	1.5	3448	6	3433	3373	16
H	Aragonite	157	7788	1887	1271.7	2.3	0.071	0.00011	4810.1	25.8	3457	6	3454	3394	7
H	Aragonite	132	8000	3402	1277.8	2.3	0.071	0.00011	2772.0	8.4	3488	6	3482	3422	8
H	Aragonite	108	7646	10,641	1242.2	2.3	0.071	0.00012	847.4	0.9	3545	7	3527	3467	19
H	Aragonite	75	6684	14,261	1229.8	2.2	0.072	0.00011	555.7	0.4	3584	7	3556	3496	29
H	Aragonite	50	7458	6707	1237.7	2.2	0.073	0.00012	1332.1	1.5	3610	7	3598	3538	14
H	Aragonite	6	4775	20,773	1232.6	2.3	0.075	0.00012	285.2	0.2	3749	7	3692	3632	57
I	Aragonite	406	5163	14,025	1348.4	2.4	0.039	0.00005	235.7	0.6	1821	3	1787	1727	34
I	Aragonite	297	6390	1607	1289.1	2.3	0.040	0.00007	2595.6	55.6	1905	4	1902	1842	5
I	Aragonite	51	7425	2100	1306.1	2.3	0.046	0.00005	2659.8	29.0	2183	3	2179	2119	5
J	Aragonite	270	5945	5236	802.5	1.8	0.137	0.00017	2575.1	13.3	8705	15	8691	8631	20
J	Aragonite	112	5690	31,482	815.4	1.9	0.140	0.00020	418.5	0.6	8830	16	8741	8681	90
N	Aragonite	460	8669	4687	878.0	1.9	0.047	0.00006	1426.7	17.1	2756	5	2747	2687	6
N	Aragonite	223	10,333	14,524	844.5	1.9	0.047	0.00006	556.3	1.7	2845	5	2823	2763	12
N	Aragonite	25	3982	5123	899.7	1.9	0.051	0.00009	653.0	9.4	2971	6	2951	2891	12
O	Aragonite	435	7616	10,988	858.1	1.9	0.026	0.00005	293.2	2.3	1518	3	1495	1435	23
O	Aragonite	160	11,156	2925	860.5	1.9	0.028	0.00004	1794.8	37.5	1688	3	1683	1623	5
O	Aragonite	39	7809	4611	863.7	1.9	0.030	0.00005	833.4	10.3	1762	3	1753	1693	10
P	Aragonite	495	8539	14,907	871.0	1.9	0.031	0.00005	295.0	1.7	1838	4	1811	1751	27
P	Aragonite	405	6233	2774	895.9	1.9	0.032	0.00005	1181.8	28.7	1853	4	1846	1786	8
P	Aragonite	381	7594	13,881	850.4	1.9	0.031	0.00005	283.0	1.8	1867	4	1838	1778	29
P	Aragonite	229	7440	15,031	895.0	1.9	0.035	0.00013	284.3	1.4	2026	8	1995	1935	32
P	Aragonite	54	6754	17,352	831.1	1.8	0.035	0.00004	225.1	0.5	2112	3	2071	2011	41

[a] $\delta^{234}U_{meas'd} = [(^{234}U/^{238}U)_{meas'd}/(^{234}U/^{238}U)_{eq}-1] \times 10^3$, where $(^{234}U/^{238}U)_{eq}$ is secular equilibrium activity ratio: $\lambda_{238}/\lambda_{234} = 1.0$. Values are reported as permil.
[b] Errors are at the 2σ level.
[c] The initial $^{230}Th/^{232}Th$ atomic ratio of $4.4 \times 10^{-6} \pm 4.4 \times 10^{-6}$ was used to correct measured $^{230}Th/^{232}Th$ ratios.
[d] Present is defined as the year 1950 AD.

and (iv) for northern Australia, the appeal is to more coarse resolution proxy data sets with inferences ranging from relatively stable middle-to-late Holocene monsoon activity (Wyrwoll et al., 1992) to an ENSO-driven collapse of monsoon precipitation during the late Holocene (McGowan et al., 2012), and with earlier claims of more general changes of enhanced El Niño-related drought during the late Holocene (e.g., Shulmeister and Lees, 1995; Shulmeister, 1999) (sites indicated in Fig. 1).

Developing a detailed and integrated understanding of the mechanisms that forced Holocene IASM variability requires continuous, high-resolution, precisely dated, IASM-sensitive records from sites across northern Australia and the Maritime Continent. Tropical Australia lies at the southern margin of the IASM system, near the location of the austral summer ITCZ, and thus is especially sensitive to IASM variability. Here we present a record of IASM variability based on oxygen isotopic ratios of stalagmites from cave KNI-51, tropical Western Australia – the first such record from tropical Australia – that spans the last 9 ka. Dating by ^{230}Th methods provides a robust and detailed chronology that offers unprecedented insight into the nature, timing, and drivers of Holocene IASM variability.

2. Geologic and environmental setting

2.1. The northwest Australian monsoon

The speleothems presented in this study were collected from cave KNI-51 (15°18'S, 128°37'E, ~100 m elevation) located in the

Ningbing Range of the eastern Kimberley region of Western Australia, an area impacted by the northwest Australian monsoon, a subset of the IASM. The climate record from Kununurra Research Station, located some 40 km south of the cave gives: mean annual maximum (minimum) temperature 35.1 °C (20.7 °C); mean annual rainfall 838 mm, with the highest (lowest) annual 1564 mm (424 mm); 90% of the mean annual rainfall is received during the period November–March. Droughts occur at approximately decadal time scales, with some of the driest episodes coinciding with El Niño events although the IASM response to El Niño is typically muted (www.bom.gov.au, Fig. 2). Tropical cyclones play an important role in regional moisture budgets, making a significant contribution to summer precipitation (Jiang and Zipser, 2010). For the wider Australian region, the reduction in tropical cyclone occurrence during El Niño events has been long recognized (Nicholls, 1979; Nicholls, 1985; Revell and Goulter, 1986; Nicholls, 1992), but the relationship between ENSO and tropical cyclones is relatively weak for the western Australian region (Broadbridge and Hanstrum, 1998).

The Australian summer monsoon usually commences during middle – late December, with the onset corresponding with a poleward displacement of the subtropical jet and ridge (McBride, 1987). Strong convection embedded in the westerly flow extends over a large region, and includes tropical cyclones and monsoon depressions. During the active monsoon, the monsoon trough is stationed over northern Australia and separates trade wind easterlies on its southern side from westerly winds between the monsoon trough and the equator (McBride, 1987). Over northwestern Australia, a stronger monsoon corresponds to location of the monsoon trough near the Pilbara Heat Low, while a weaker monsoon corresponds to a more equatorward location of the monsoon trough (Suppiah, 1992; Moise and Colman, 2009). Over the region of the Maritime Continent, high SST associated with the IPWP provide a broad area of strong convection that results in a more diffuse and less well-defined ITCZ than over the adjacent Pacific and Indian oceans (Walliser and Gautier, 1993). At seasonal time scales, the effectiveness of the IASM over northwestern Australia relates to the strength of the westerly inflow and attendant moisture fluxes into the monsoon trough via the ITCZ (Suppiah, 1992; Wheeler and McBride, 2011). In a general sense, the structural definition of the ITCZ over the adjacent Indian Ocean is a guide to the strength of the westerly inflow into the monsoon region of northwestern Australia.

Other factors influencing IASM precipitation include the Madden-Julian Oscillation (MJO) that impacts the strength of westerly flow into the monsoon trough (Wheeler et al., 2009;

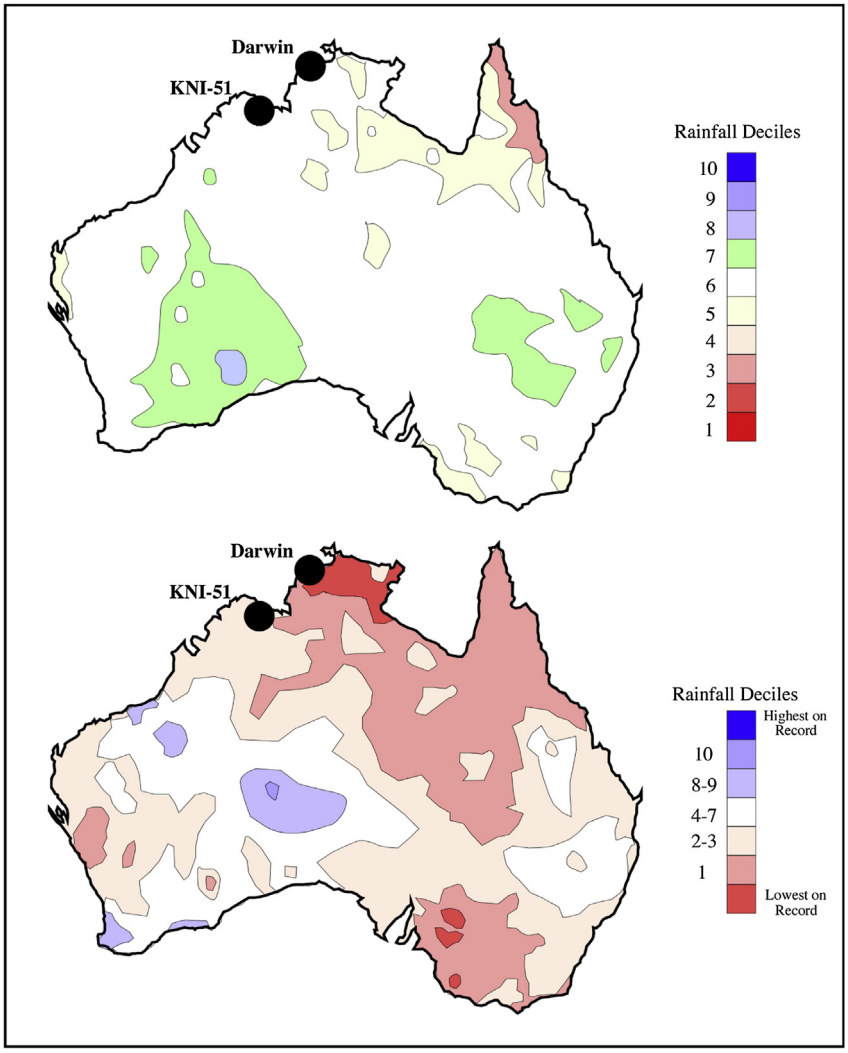

Fig. 2. Top - Summer (DJF) mean rainfall deciles associated with twelve 20th Century moderate-strong canonical El Nino events. Bottom – Summer (DJF) mean rainfall deciles for exceptionally strong El Nino event of 1982/1983. After figures presented at http://www.bom.gov.au/climate/enso/ninocomp.shtml.

Wheeler and McBride, 2011); much of the variability in summer rainfall is linked to the occurrence of MJO events. Another (related) control includes the build-up and subsequent drawn-down of the Siberian high that produces large atmospheric transfer (cold surges) between the Northern and Southern hemispheres, triggering deep convection over the Maritime Continent (Slingo, 1998; Chang et al., 2004, 2006; Wheeler and McBride, 2011), events capable of leading to the flare-up of active monsoon phases over northwestern Australia (Suppiah and Wu, 1998; Hong and Li, 2009) and possibly influencing the structure and location of the ITCZ over the wider Indian Ocean. While the impact of cold surges on convection over the Maritime Continent is well known, less well recognized is the role of cold surges emanating out of west Asia, which lead to deep convection to the north of Madagascar, and amplify MJO convection (Wang et al., 2012). Through this a link is established between the western Indian Ocean, a well defined structure of the ITCZ and associated MJO events and active phases over the IASM region – strongly exemplified by January–February 2008 events (Wang et al., 2012). The IOD is an atmosphere-ocean coupling (Saji et al., 1999) linked to IASM variability in Flores (Griffiths et al., 2010), but given that IOD events typically form, peak, and decay during the austral winter and spring, their impact on IASM rainfall in the eastern Kimberley is limited (Taschetto et al., 2011; www.bom.gov.au).

One of the most important factors influencing Australia-wide precipitation trends is ENSO. El Niño events involve an eastward shift of warm IPWP surface waters that, in turn, alter the Walker circulation and reduce atmospheric convection over the Indo-Pacific region. But while the IPWP is the center of action for ENSO, and these events clearly influence rainfall in many parts of Australia (e.g. McBride and Nicholls, 1983; Hendon et al., 2012), the impact of ENSO on the summer monsoon rainfall regime of northwestern Australia is muted (McBride and Nicholls, 1983; www.bom.gov.au; Fig. 2). While La Nina events can have a strong rainfall signal over this region and are characterized by increased austral spring/summer rainfall (www.bom.gov.au), analysis of SST in NINO3.4 show minimal effects of El Niño in the eastern Kimberley except during exceptionally strong events (Figs. 1 and 2). Strong El Niño events (for instance, austral summer 1982/83) may result in pronounced droughts over northwestern Australia, an effect possibly amplified by a positive correlation between IPWP SST and pre-monsoon onset (SON) rainfall in tropical Australia, which accounts for upwards of 30% of total wet season rainfall overall but only ~10% in the eastern Kimberley (www.bom.gov.au; Hendon et al., 2012). El Niño Modoki events represent a newly identified and poorly understood phenomenon which impacts rainfall across the Indo-Pacific somewhat differently than do conventional El Niño events (Ashok et al., 2007), and in general shorten but intensify the monsoon season over northwestern Australia (Taschetto and England, 2009). However, it remains unclear whether stronger and/or more frequent El Niño events, such as are thought to have occurred in the late Holocene (Moy et al., 2002) may have taken on more of a steering role for the northwest Australian summer rainfall regime.

The likelihood that ENSO-rainfall relationships have changed over time is generally recognized (e.g., Webster and Palmer, 1997) and raises the possibility that a stronger coherence between ENSO and IASM rainfall may have existed at different intervals of the Holocene. This contention is supported by analysis of historical rainfall data, SOI indexes, and western Pacific SST that suggest that the relationship between ENSO and IASM rainfall appears to have been dynamic across the monsoon regions of tropical Australia over (multi)decadal time scales. For example, Nicholls and Coauthors (1996) documented a shift toward higher Australia-wide average maximum temperatures and rainfall for a given value of SOI since the early 1970s relative to earlier decades, and suggested a connection to Indian Ocean SST. Latif et al. (1997) found a strong relationship between the Pacific Decadal Oscillation (PDO) and IASM rainfall, a result that was further explored by Power et al. (1999) who documented a multidecadal modulation of ENSO and its effects on Australia rainfall (the Interdecadal Pacific Oscillation, IPO). The IPO has positive and negative phases, with the former yielding weak relationships between SOI and Australian climate, while the latter involves strong correlations. More recently, Wu and Kirtman (2007) modeled the role played by Indian Ocean SST on the ENSO-IASM relationship and found that higher correlations occur during periods with larger ENSO amplitude. The PDO and IPO involve changes in the mean state of tropical Pacific SST, and hence a shift in the Walker circulation and mean location of convection. Similar mean state changes may have occurred on millennial time scales, modulating ENSO impacts on northern Australian rainfall.

2.2. Cave KNI-51 and regional geology

Two calcite and seventeen aragonite stalagmites were collected from cave KNI-51. The Ningbing Range is composed of alluviated labyrinth karst formed in Devonian limestone with relief of approximately 60–80 m (Kiernan, 2004). Numerous caves cross-cut these hills, each sharing similar features including shallow depths, small openings, and quasi-horizontal passageways connecting modestly decorated rooms. Cave KNI-51 is shallow, lying within 15 m of the land surface at its deepest point, and is approximately 600 m in length; the two calcite stalagmites, KNI-51-0 and KNI-51-4, were collected in a dead-end passage at the rear of the cave while the aragonite stalagmites were collected approximately 100 m from the end of the passage. Soils over the caves are thin, and limestone bedrock karst is exposed through the area's eucalyptus savanna. When visited in June 2009 and June 2011, cave temperatures were approximately 28 °C with high humidity and no active drips, suggesting that infiltration through the overlying bedrock requires less than two months, the time elapsed since the end of the previous monsoon season.

3. Analytical methods

3.1. U/Th Stalagmite chronology

Each stalagmite was sectioned along its vertical growth axis using a water-cooled saw and inspected for signs of recrystallization. The calcite stalagmites are composed of fibrous elongate crystals with no visible signs of diagenetic alteration, but several of the aragonite stalagmites contain zones that have been altered to coarsely crystalline calcite cutting diachronously across multiple growth horizons. These layers are easily identified and were not sampled for either stable or radiogenic analysis.

Stalagmites were dated using ^{230}Th techniques at the University of New Mexico Radiogenic Isotope Laboratory. Samples ranging from 50 to 150 mg were milled from the central growth axis using a computer-guided micromill and transferred into Teflon beakers for processing. Powders were dissolved in 15N nitric acid, spiked with a mixed ^{229}Th–^{233}U–^{236}U tracer, and this solution was dried on a hot plate. A mixture of nitric and perchloric acids was then used to oxidize any organic matter, and the solution was dried, redissolved in 7N nitric acid, and processed using standard column chemistry methods. The isolated U and Th fractions were dissolved in 4 ml of 3% nitric acid and transferred to analysis tubes for measurement on a Thermo NEPTUNE multi-collector inductively coupled plasma mass spectrometer (MC-ICP-MS). U and Th isotopic ratios were measured separately by being aspirated into the MC-ICP-MS using a Cetac Aridus II low flow desolvating nebulizer system and run as

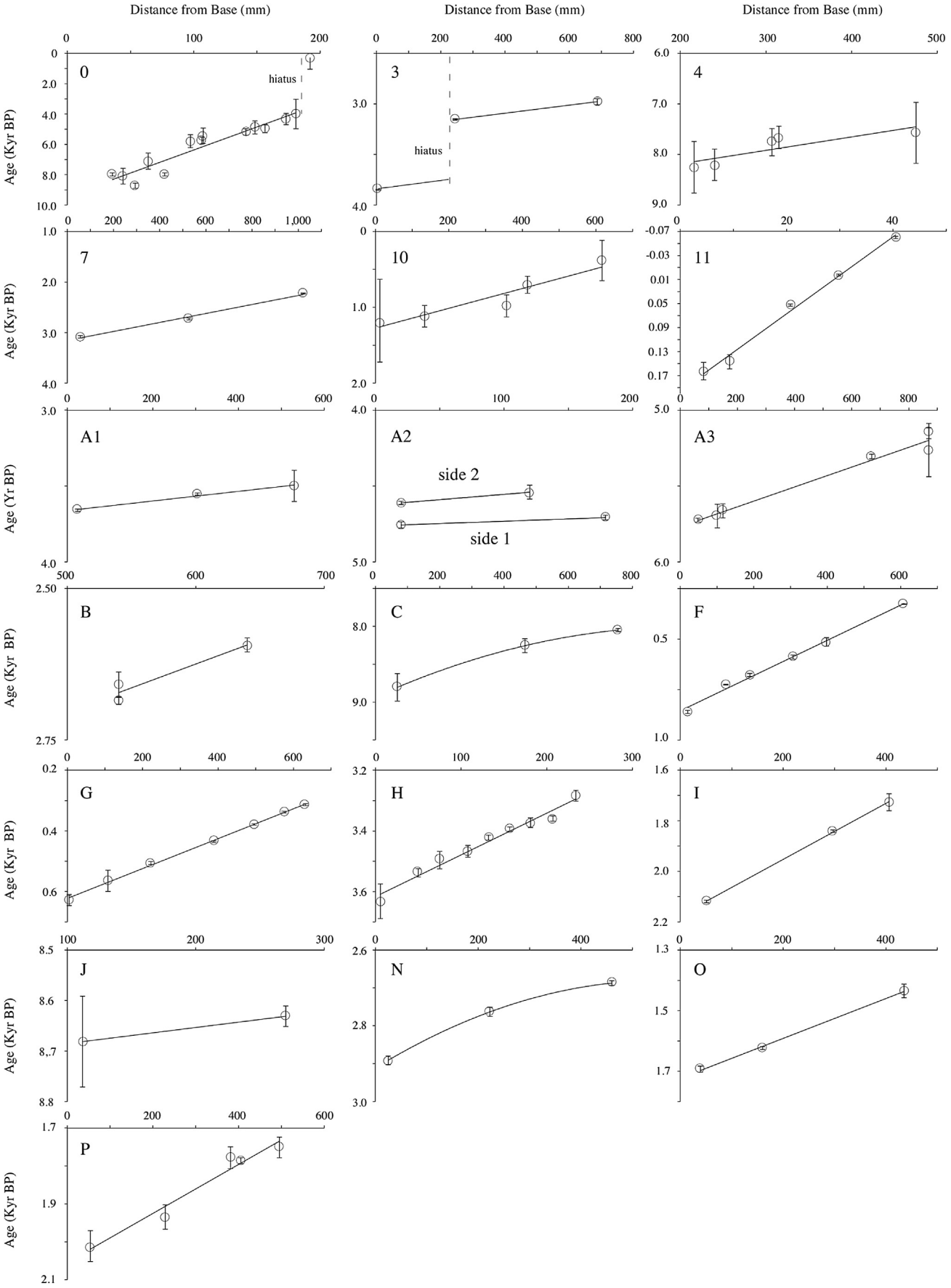

Fig. 3. Growth models of KNI-51 stalagmites. Sample names are listed in the upper left of each panel. Vertical bars represent two standard deviation errors, many of which are smaller than the symbol denoting the position of the dated interval.

static routines. For the aragonite stalagmites, all U isotopes of interest (^{238}U, ^{236}U, ^{235}U, ^{234}U, and ^{233}U) and ^{232}Th and ^{229}Th were measured in Faraday cups, while ^{230}Th was measured in the secondary electron multiplier (SEM). Run conditions were similar for the calcite samples, except that ^{234}U was measured on the SEM. Gains between the SEM and the Faraday cups were determined using standard solutions of NBL-112 for U and an in-house ^{230}Th–^{229}Th standard for Th which was measured after every fifth sample; chemistry blanks reveal U and Th blanks below 20 pg. Decay constants used are those reported by Cheng et al. (2000). Unsupported ^{230}Th was corrected by applying the average crustal silicate ^{230}Th/^{232}Th ratio of 4.4 ppm ± 4.4 ppm. Ages are reported using two standard deviation errors and are adjusted to the year AD 1950 as present.

3.2. Stable isotopic analyses

For stable isotopic analysis, powders were milled using a handheld drill from the central axis of each stalagmite. Stable isotopic ratios were obtained at the Iowa State University Department of Geological and Atmospheric Sciences and the University of Michigan Department of Earth and Environmental Sciences. At Iowa State University, isotopic ratios were measured with a GasBench II with a CombiPal autosampler coupled to the inlet of a ThermoFinnigan Delta Plus XL continuous flow mass spectrometer. At the University of Michigan, samples were analyzed using a Finnigan MAT 253 coupled with an automated carbonate preparation device (Kiel III). All oxygen and carbon isotopic values are presented in parts permil (‰) relative to the Vienna PeeDee Belemnite carbonate standard (VPDB). Precision was determined by the regular analysis of standards interspersed among the samples and is better than 0.1‰ for oxygen. Replication between the two labs is excellent, and data from both labs are thoroughly integrated.

3.3. Controls on regional precipitation and KNI-51 dripwater $\delta^{18}O$ values

No rainwater or cave dripwater monitoring has been conducted at KNI-51, and the Global Network of Isotopes in Precipitation (GNIP) station nearest to KNI-51 is located approximately 400 km to the northeast at Darwin, Northern Territory (Fig. 2). Oxygen isotopic (δ^{18}O) analyses of rainfall at Darwin reveal a strong correlation with monthly rainfall amount ($R^2 = 0.8$; $p < 0.001$) (−1‰/100 mm/month), and thus the IASM rainfall variability is reflected in rainwater oxygen isotopic ratios due to amount effects (Dansgaard, 1964; IAEA/WMO). Unlike related regional studies from Indonesia (Griffiths et al., 2009, 2010) and Borneo (Cobb et al., 2007; Partin et al., 2007), moisture source variations are limited in the Kimberley, and thus do not account for a significant portion of inter- or intra-annual precipitation δ^{18}O variations (Suppiah, 1992).

Infiltrating meteoric fluids contribute the vast majority of the oxygen contained in stalagmite carbonate (Hendy, 1971), and because rainwater δ^{18}O values are dominated by amount effects in this region, stalagmite oxygen isotopic ratios should also track monsoon activity. Equilibrium oxygen isotopic fractionation associated with calcite and aragonite crystallization is −0.2‰/°C (Tarutani et al., 1969; Kim and O'Neil, 1997) and thus during climatically stable periods such as the Holocene, temperature change was responsible for imparting little isotopic variability to speleothem carbonate. We therefore apply the method of several previous (sub)tropical speleothem studies by interpreting our stalagmite δ^{18}O time series as reflecting changes in rainwater δ^{18}O values which, in turn, track monsoon strength (Wang et al., 2001, 2005; Partin et al., 2007; Cosford et al., 2008; Griffiths et al., 2009, 2010).

4. Results

4.1. Fidelity of the paleomonsoon record

A total of 92 ^{230}Th dates was obtained from the nineteen KNI-51 stalagmites, and growth models were constructed using polynomials fit through these data (Fig. 3). The calcite and aragonite stalagmites at KNI-51 offer a dramatic contrast in terms of their suitability for ^{230}Th dating. While both contain similar δ^{234}U values, U concentrations are approximately 100 times higher in aragonite stalagmites than their calcite counterparts (5 ppm vs 50 ppb), and thus errors on the aragonite stalagmite ages are considerably smaller than for calcite stalagmites. Deposition of calcite is confined largely to the early and middle Holocene, while the late Holocene is dominated by aragonite.

Although diagenetically altered areas were easily identified and carefully avoided, we assessed the possible effects of recrystallization on the aragonite stalagmite chronology by dating unaltered and recrystallized portions of the same growth layers in stalagmite KNI-51-3. Loss of U and subsequent age discordance has been observed in speleothem calcite formed by recrystallization of aragonite (Ortega et al., 2005; Lachniet et al., 2012). Here, however, original aragonite dated to 5.20 ± 0.05 ka while the coeval recrystallized calcite portion yielded an age of 5.34 ± 0.16 ka, within error of the unaltered portion and indicating that small amounts of calcite included in powders milled for dating would not have noticeably impacted the chronology.

The KNI-51 record is composed of a total of 1497 stable isotope analyses but the utility of KNI-51 stalagmites as paleomonsoon proxies rests on the ability of stalagmite carbonate to accurately preserve amount effect-driven changes in the δ^{18}O values of infiltrated IASM rainwater. Evaluating the degree of equilibrium crystallization in these stalagmites is therefore an important step. In tropical settings, a variety of mechanisms can force the oxygen isotopic values of speleothem carbonate away from equilibrium, including effects that occur prior to and during infiltration, as well as during carbonate precipitation on the stalagmite surface. Mickler et al. (2004) documented stalagmite δ^{18}O values that were both higher and lower than equilibrium based on coupled analysis of modern cave temperature, dripwater δ^{18}O, and calcite δ^{18}O values, demonstrating the need to evaluate each stalagmite independently.

When crystallization temperature and cave dripwater δ^{18}O values are not known, the most reliable test for equilibrium carbonate precipitation involves comparing the isotopic values and trends in coeval stalagmites (Denniston et al., 1999; Dorale and Liu, 2009). The crystallization of aragonite and calcite mineral phases in speleothems has been linked to dripwater chemistry, typically Mg/Ca ratios, that may reflect hydrologic/climatic conditions, with aragonite tied to increased aridity (Bar-Matthews et al., 1991; Railsback et al., 1994; de Choudens-Sánchez and González, 2009). In order to compare the oxygen isotopic values of calcite and aragonite, calcite δ^{18}O values were increased by 1‰ to account for the differential oxygen isotopic fractionation of aragonite and calcite (Bohm et al., 2000). The magnitude of this offset is within the range of oxygen isotopic fractionation differences observed between synthetic aragonite and calcite (Tarutani et al., 1969; Kim and O'Neil, 1997; Kim et al., 2007) as well as aragonite and calcite mollusc shells (Lécuyer et al., 2012).

The fidelity of the KNI-51 times series as a paleomonsoon proxy is supported by the excellent overlap of δ^{18}O values in coeval stalagmites, including aragonite and calcite sections (Fig. 4). Only one stalagmite, KNI-51-11, did not grow at the same time as another stalagmite from this cave, but this sample was active when collected and thus aragonite δ^{18}O values from the most recently deposited aragonite were used to calculate crystallization

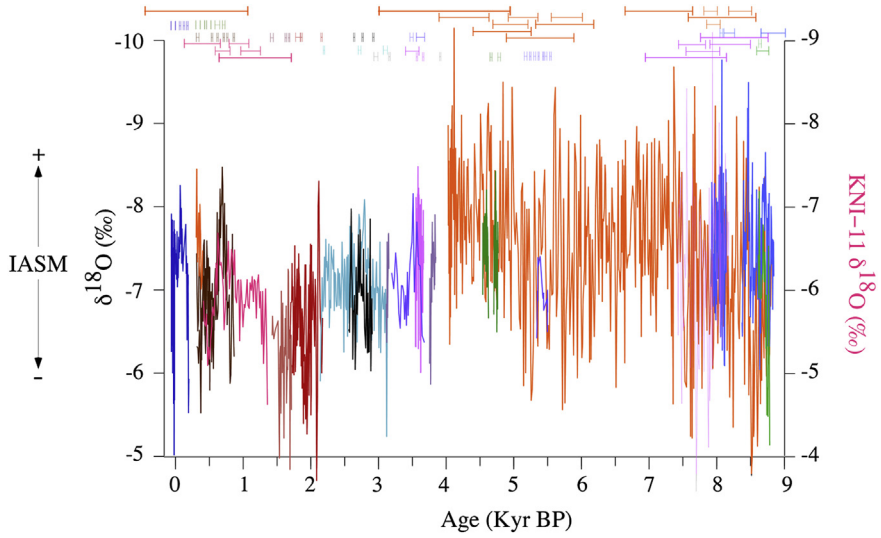

Fig. 4. Full stable isotope time series of KNI-51 stalagmites, each of which is represented by a different color. Horizontal bars mark two standard deviation error windows on ^{230}Th ages. KNI-51-10 is plotted on separate (righthand) vertical axis to account for 1‰ offset in oxygen isotopic ratios. Calcite oxygen isotopic ratios adjusted by 1‰ to account for differential isotopic fractionation between calcite and aragonite (Bohm et al., 2000); see text for details.

temperatures as a test for isotopic equilibrium. Because no rainwater δ^{18}O values for precipitation are available at this site, we used average rainwater δ^{18}O values from the GNIP station at Darwin. Using the modified temperature equation of Craig (1965), these data yield crystallization temperatures of 27 ± 2 °C, within error of regional mean annual temperature (28 °C) that, while by no means definitive, suggest isotopic equilibrium crystallization in this sample. Only one stalagmite, KNI-51-10, is characterized by δ^{18}O values that do not overlap with stalagmites of the same age; this sample contains oxygen isotopic ratios ~1‰ higher than two other stalagmites that grew synchronously. The origin of this offset is unclear given that KNI-51-10 formed in the same room as the other aragonite samples, although variations in dripwater chemistry and growth conditions have been observed over similar spatial scales in other tropical settings (Mickler et al., 2004). However, the KNI-51-10 δ^{18}O time series is characterized by variations that are identical to those occurring in coeval samples, and we therefore included KNI-51-10 in our record after decreasing the KNI-51-10 δ^{18}O values by 1‰ to match the other two coeval stalagmite δ^{18}O time series (Fig. 4).

4.2. Millennial-scale IASM variability

The KNI-51 oxygen isotopic time series reveals a dynamic and variable Holocene monsoon at the southern margins of the IASM system. In the early Holocene, stalagmite δ^{18}O values decreased from −7.5 to −8.5‰ between 9 and 7 ka, reflecting enhanced amount effects on precipitation oxygen isotopic ratios and marking increases in monsoon rainfall. This response was similarly observed in other records from the IASM region (Partin et al., 2007; Griffiths et al., 2009) and attributed to flooding of the Sahul and Sunda continental shelves (Griffiths et al., 2009). Overall, the KNI-51 record defines a greater range in Holocene δ^{18}O values than does either the Flores or Borneo stalagmite records, but the degree of early Holocene IASM strengthening at KNI-51 is muted relative to sharp increases observed over the same period at Flores and Borneo (Fig. 5). For the northwestern Australia region, modeling studies have suggested the importance of tilt and SST in leading to strong monsoon flow, particularly during times of low latitude Southern Hemisphere insolation minima such as in the latest Pleistocene-earliest Holocene (Liu et al., 2003; Wyrwoll et al., 2007). Despite evidence for influences of North Atlantic climate and oceanic thermohaline circulation on the Holocene EASM (Wang et al., 2005), no clear isotopic anomalies are apparent (even within the age uncertainties) with periods of reduced thermohaline circulation such as the 8.2 ka event (Alley et al., 1997).

The middle Holocene (7.5–4.5 ka) was a period of overall enhanced IASM rainfall in the eastern Kimberley, with average KNI-51 stalagmite δ^{18}O values between −8 and −9‰. A consistent and strengthened middle Holocene IASM has been suggested from plunge pool sediments in the Northern Territory (located east of the Kimberley) (Nott and Price, 1994) where peak rainfall was marked from 8 to 4 ka, and the middle Holocene was also a period of rainforest expansion across the Australian tropics and southern IPWP (Hiscock and Kershaw, 1992; Shulmeister, 1999; Genever et al., 2003; Rowe, 2007). Within this period of overall elevated rainfall, a gradual shift toward higher δ^{18}O values from 7.0 to 5.5 ka marks a period of reduced IASM strength at KNI-51, followed by a return to peak monsoon rainfall from 5 to 4 ka. Some regional records suggest that the IASM was weakened and/or variable during this time. For example, increased aridity from 6.3 to 4.5 ka was documented through a recent pollen and sedimentological analysis of a middle and late Holocene spring deposit located in the Kimberley west of KNI-51 (McGowan et al., 2012). A substantial middle Holocene weakening of the IASM is also recorded in the Flores stalagmite record, and in fact, the Flores time series exhibits a well-defined anti-phasing with the KNI-51 record during this interval (Fig. 6), including a prominent IASM rainfall minimum (maximum) in the Kimberley (Flores) records from 6.5 to 5.5 ka, and a rainfall maximum (minimum) from 5 to 4 ka. This anti-phasing continues into the late Holocene, with a secular shift toward a weaker (stronger) monsoon beginning at 4 ka. In contrast, the KNI-51 and Borneo time series experienced in-phase IASM variability, including a plateau in IASM strength from 6.5 to 5.5 ka, peak IASM rainfall from 5 to 4 ka, and decreasing IASM strength beginning at 4 ka. Griffiths et al. (2010) noted similarities between Flores and Borneo stalagmite δ^{18}O trends during the early and late Holocene, and an inverse correlation during the middle Holocene which they tied to IOD-driven contraction or migration of the IPWP and resulting changes in SST patterns and shifted centers of

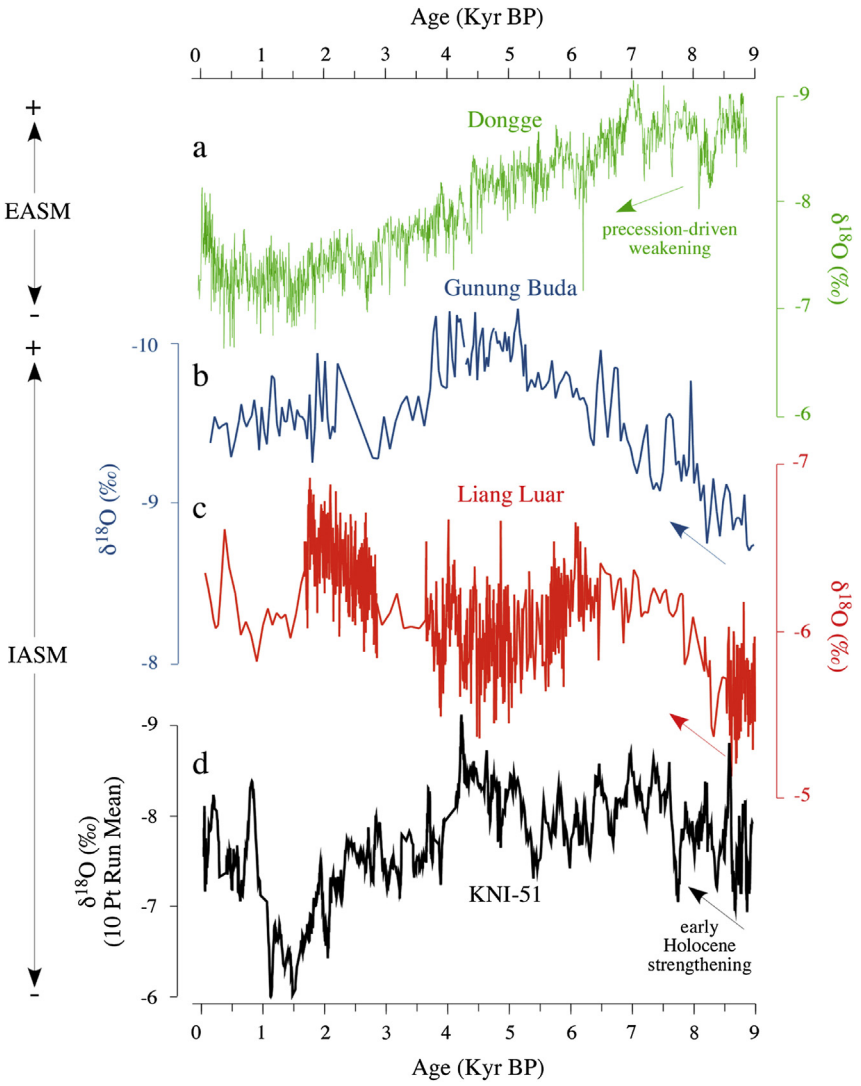

Fig. 5. Holocene monsoon reconstructions from stalagmite oxygen isotopic ratios at Dongge Cave, China (Wang et al., 2005), Gunung Buda, Borneo (Partin et al., 2007), Liang Luar, Flores (Griffiths et al., 2009), and KNI-51 (this study). KNI-51 data are presented as running mean and gaps between non-overlapping stalagmites are omitted.

atmospheric convection. McGowan et al. (2012) linked pollen and charcoal data from Black Spring, also located in the Kimberley, to increases in the frequency of severe drought in the middle/late Holocene and a resulting hiatus in Aboriginal habitation from a 5–4 ka.

The transition from the middle to late Holocene is marked by the most prominent feature of the KNI-51 time series: a dramatic and sustained weakening of monsoon rainfall marked by a 2‰ increase in $\delta^{18}O$ values from 4.2 to 1.5 ka, with peak aridity centered from 1.5 to 1.2 ka. This interval is followed by a sharp 1.5‰ decrease from 1.2 to 0.9 ka that indicates a return to wetter conditions that persisted, with continued smaller-scale variability, throughout the last millennium. Given that the early and middle Holocene record at KNI-51 is dominated by calcite, and the late Holocene record is dominated by aragonite, the structure of the oxygen isotopic trend at 4 ka is dependent, in part, on the correction for fractionation differences between these two mineral phases and for which some uncertainty exists. However, these uncertainties are capable only of slightly reducing the magnitude of this shift, and not the shape of the overall trend, in the KNI-51 $\delta^{18}O$ curve. In fact, the transition from calcite to aragonite as the dominant mineral phase may itself suggest an increasingly weakened or unstable IASM in the late Holocene.

5. Origins of IASM variability

With the availability of the KNI-51 data and these high-resolution proxy records, it may now be possible to frame hypotheses related to forcing controls of the evolution of the full IASM system during the Holocene. In the eastern Kimberley, statistical correlations between IPWP SST and IASM (DJF) rainfall are near zero to weakly negative (Hendon et al., 2012), and the IOD plays little role in IASM rainfall variability. Thus the proposed IOD mechanism used to explain anti-phasing between Flores and Borneo (Griffiths et al., 2010) cannot easily be applied to the eastern Kimberley, and suggests a different origin at both sites.

An alternative mechanism involves meridional shifts in the austral summer ITCZ. Meridional shifts in the ITCZ band may be pronounced, even during the Holocene. Based on analysis of lake sediments on islands spanning the tropical Pacific, Sachs et al. (2009) argued for a southward migration of the Pacific ITCZ of 5° latitude during the Little Ice Age. The Dongge Cave record reveals a clear Holocene-long weakening of the EASM in southern China that reflects insolation-driven changes in the heat balance between the Northern and Southern Hemisphere tropics and a concomitant southward migration of the ITCZ (Wang et al., 2005) (Fig. 5). And Newton et al. (2006) tied IPWP SST and salinity variations over the

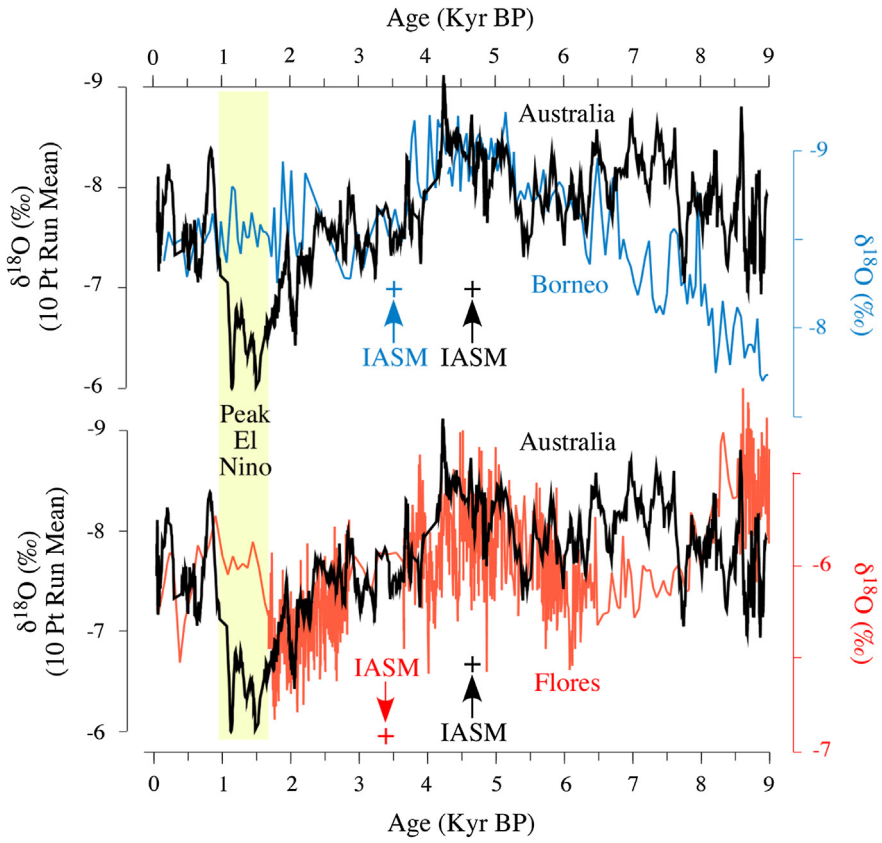

Fig. 6. Overlap of Gunung Buda, Borneo and Liang Luar, Flores oxygen isotopic time series with that of cave KNI-51. Note differential phasing of IASM rainfall between KNI-51 and these two sites. KNI-51 data are presented as running mean and gaps between non-overlapping stalagmites are omitted.

past millennium to migration of the ITCZ. Positioning of the ITCZ has been tied to high northern latitude climate, with decreased temperatures (Broccoli et al., 2006) and/or increased ice cover (Chiang and Bitz, 2005) linked to its southward displacement. A southward shift in mean ITCZ position would have increased rainfall in the Kimberley, and rising austral summer insolation throughout the Holocene would have favored such a change.

Meridional displacement of the ITCZ does not readily explain the observed relationships between KNI-51 with sites from across the IPWP and the broader Pacific, however. For example, based on reconstructed eastern and western tropical Pacific SST, Koutavas et al. (2006) argued for a *northward* shift in mean ITCZ position during the middle Holocene as a means of explaining an increased zonal temperature gradient between 8 and 4 ka. In addition, given the close proximity of Flores and the Kimberley, as well as the diffuse structure of the ITCZ in the IPWP, it is difficult to explain the observed phasing of IASM activity at these sites by mean position changes in the ITCZ. Evidence against ITCZ displacement as an explanation for the observed Holocene IASM records also comes from a stalagmite-based paleomonsoon reconstruction from Ball Gown Cave in the western Kimberley that spanned the last deglaciation (Denniston et al., 2013). At Ball Gown Cave, the IASM strengthened markedly during periods of pronounced North Atlantic cooling such as the Younger Dryas and Heinrich Stadial 1, a response consistent with sites from the southern IPWP, including Flores (Griffiths et al., 2009; Muller et al., 2012) and opposite in sign to sites from Asia and the northern IPWP, including Borneo (Wang et al., 2001; Partin et al., 2007). These relationships suggest a southward migration of the ITCZ band during these times. During the Holocene, however, the phasing between the Kimberley, Borneo, and Flores is reversed, suggesting a different mechanism drove IASM variability in the Holocene.

Diminished late Holocene IASM rainfall recorded at KNI-51 is similar to other regional data from tropical Australia and the IPWP suggesting a weakened and more variable IASM at this time and has been tied to an increase in the frequency and/or amplitude of El Niño events since ~5 ka (McGlone et al., 1992; Shulmeister, 1999; Haberle and Ledru, 2001; Gagan et al., 2004; McGregor and Gagan, 2004; Asmussen and McInnes, 2013) as well as sites from across the Pacific (Koutavas and Joanides, 2012). In north-central Australia, Shulmeister and Lees (1995) documented pollen evidence for more frequent late Holocene drought, and Haberle and Ledru (2001) linked increases in charcoal abundance in late Holocene sequences from Papua-New Guinea and Indonesia to increased frequencies of burning thought to have originated, in part, from El Niño-related drought (Fig. 7). And pollen analysis from the Kimberley by McGowan et al. (2012) tied an inferred reduction in rainfall from 6.3 to 4.5 and 2.4 to 1.3 ka to ENSO. None of these proxy records can directly address changes in ENSO frequency or amplitude because they do not resolve annual time scales (Cane, 2005), but changes in the mean amplitude or frequency of ENSO events may occur on longer time scales and these may impact regional rainfall/monsoon-related climates.

High-resolution records of ENSO variability during the Holocene include lake records from Laguna Pallchachoca from South America (Moy et al., 2002) and El Junco Crater Lake in the Galapagos Islands (Conroy et al., 2008). At Laguna Pallchachoca, El Niño events are linked to increased sediment influx, analysis of which argues for an amplification of El Niño activity ramping up at ~4 ka and peaking at 1 ka before diminishing significantly to the present. At El Junco,

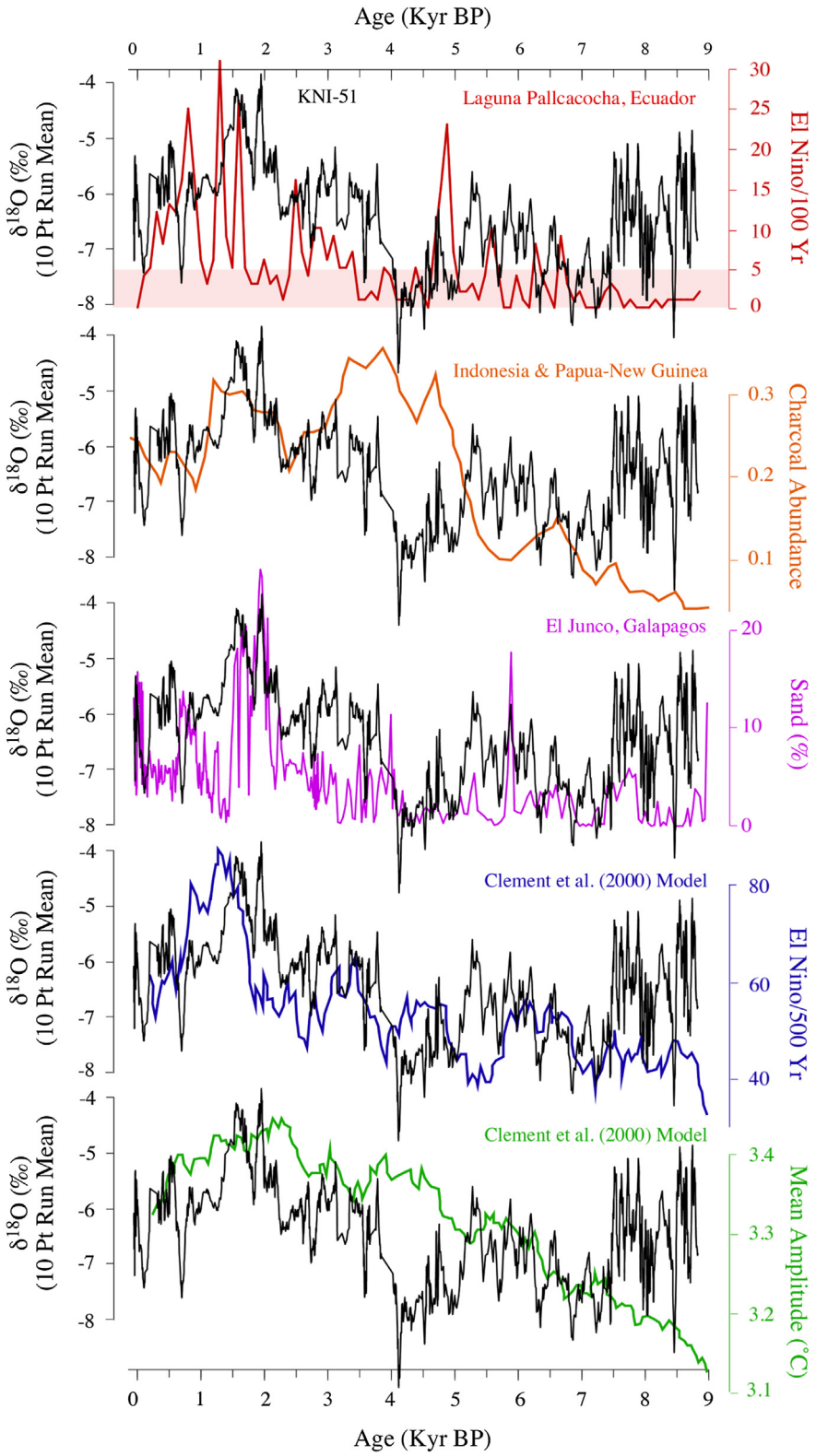

Fig. 7. Comparison of KNI-51 oxygen isotopic time series with Holocene El Nino reconstructions and models from Pacific Basin sites. From top to bottom: Laguna Pallcacocha, Ecuador (Moy et al., 2002); Indonesia and Papua-New Guinea (numerous sites) (Haberle and Ledru, 2001); El Junco lake, Galapagos (Conroy et al., 2008); ENSO model results (Clement et al., 2000). KNI-51 data are presented as running mean and gaps between non-overlapping stalagmites are omitted.

sediment size reflects the dominant hydroclimatic regime, with the wetter conditions that characterize El Niño events triggering increases in sediment size, and which suggest an evolution of El Niño similar to that reconstructed at Laguna Pallchachoca. Both of these reconstructions are largely consistent at millennial-scales with a model of El Niño based on orbitally-driven changes in tropical insolation, and which yields increases in both El Niño frequency and amplitude from the middle to late Holocene (Clement et al.,

2000) (Fig. 7). These El Nino-sensitive sites and the model of El Niño activity bear a visual similarity to the KNI-51 $\delta^{18}O$ time series (Fig. 7), suggesting evolution of IASM rainfall in the Kimberley was influenced by changes in ENSO amplitude or frequency over this period.

There are two problems with this model, however. First, despite the fact that IASM rainfall is impacted by ENSO at both Borneo and Flores (Chang et al., 2004, 2006; Partin et al., 2007), only the Flores record preserves evidence of substantial environmental change from 2 to 1 ka, the period of peak El Niño recorded at Laguna Pallchachoca and El Junco. Second, given the weak association of El Niño with summer monsoon rainfall anomalies in the eastern Kimberley, it appears unlikely that current relationships would allow such a pronounced reduction in late Holocene rainfall due solely to more stronger El Niño events, especially since this would also imply stronger La Nina events which can bring increased rainfall.

We see three possible mechanisms that may at least partially reconcile these apparent contradictions: (i) temporal variability in the nature of El Niño events; (ii) increases in the amplitude and/or frequency of ENSO events; and (iii) changes in the mean state of the tropical Pacific. We address each mechanism in turn.

Firstly, El Niño events are characterized by a negative SOI index and a shift in warm IPWP waters eastward across the tropical Pacific, but the spatial pattern of SST warming is highly variable. In canonical El Niño events, warm waters extend eastward through the NINO3.4 and NINO3 region (Fig. 1) into the eastern Pacific with a resulting shift in Pacific basin-wide Walker Circulation. El Niño Modoki events, however, involve the center of peak SST located further west in the central tropical Pacific with colder anomalies on either side (Ashok et al., 2007). This SST pattern establishes a two-stage Walker circulation system over the Pacific, and has been shown to produce rainfall anomalies in the IASM region of northern Australia that are distinct from those associated with traditional El Niño events (Taschetto and England, 2009). In general, the impacts of Modoki events on northwestern Australia include sharp reductions in rainfall during austral autumn (MAM), below average rainfall in December and March, and above average rainfall in January and February – in general, a shortened and intensified monsoon period (Taschetto and England, 2009). The origin and evolution of Modoki events remain under investigation, but increases in the frequency of these events in recent decades imply that they may vary in response to changes in the mean climate (Yeh et al., 2009). It is possible that similar changes in ENSO type, such as more or fewer Modoki events, may have played a role in altered late Holocene rainfall patterns across the IPWP.

Second, models of ENSO behavior (Clement et al., 2000) and El Niño reconstructions (Moy et al., 2002; Conroy et al., 2008) argue for increased El Niño frequency and/or amplitude in the late Holocene relative to the middle Holocene. Increases in the frequency of El Niño events could have reduced pre-monsoon rainfall via the strong correlation between rainfall in these months with IPWP SST (Hendon et al., 2012). Tierney et al. (2012) suggested such a mechanism as a means of reconciling their leaf wax isotopic record from Sulawasi (3°S, 119°E) (Fig. 1) with the Borneo and Flores cave records. Their data, coupled with general circulation model results, suggests that spatial heterogeneity of rainfall, particularly during the austral spring (SON), is an important component of regional moisture balances and thus may explain the differences between the Gunung Buda and Liang Luar oxygen isotopic time series. If correct, the strong correspondence between IPWP SST and austral spring rainfall in the Kimberley may provide a mechanistic link between KNI-51 and the Gunung Buda record. In addition, the exceptionally strong El Niño of 1982/83 yielded pronounced reductions in rainfall in the eastern Kimberley (Fig. 2), suggesting that at least some higher amplitude El Niño events were capable of sharply reducing IASM rainfall over tropical Australia in ways that lower amplitude events of the 20th century were not. Thus, historical records may not serve as adequate proxies for a strengthened ENSO system such as has been ascribed to the late Holocene. But changes in ENSO variance throughout the Holocene remain the subject of debate. Coral data from the IPWP offer contradictory results, with McGregor and Gagan (2004) arguing for a change in the atmospheric response to IPWP SST during the middle and late Holocene, with peak offset from 2.5 to 1.7 ka, similar to peak aridity at KNI-51 (Fig. 5), while other data suggest no discernable shift in ENSO variance over the Holocene (Cobb et al., 2013).

Third, the mean state of the tropical Pacific may have evolved during the Holocene. Historical data suggest that on decadal time scales, the IPO/PDO leads to a more La Nina-like (IPO negative) or El Niño-like (IPO positive) Pacific SST pattern, with changes in mean state enhancing La Nina events (El Niño events) and altering the strength of teleconnections between the NINO region and Australian rainfall, and there is also some evidence that ENSO amplitude may be reduced in this phase (Power et al., 1999; Arblaster et al., 2002). As such, mean state changes could produce an overall increase or decrease in northern Australian rainfall. A shift in the mean state of ENSO has been proposed for Greenland stadials (an embedded El Niño state) versus interstadials (an embedded La Nina state) (Stott et al., 2002), the Last Glacial Maximum (an embedded El Niño state), and the middle Holocene (an embedded La Nina state) (Koutavas et al., 2002).

Finally, in addition to the millennial-scale IASM variations apparent in the late Holocene, several sharp, centennial-scale variations in monsoon rainfall are also apparent (Fig. 4), many of which are similar in timing to features recorded in other regional stalagmite time series and which therefore hint at drivers of IASM variability that operate regionally on short time scales. Included in these mechanisms are solar variability and volcanic activity, as well clusterings of cold surge events that impact the organization of convection over the wider IASM region. The extremely high temporal resolution afforded by the rapid growth rates and precise ^{230}Th dates of KNI-51 aragonite stalagmites will allow a more detailed examination of sub-millennial-scale shifts in monsoon behavior that, in turn, will provide important tests for the origins of IASM variability during the Holocene.

6. Conclusions

Stalagmites from cave KNI-51 represent the first high-resolution, absolute-dated speleothem record of Holocene IASM variability from the Australian tropics. The fidelity of this record as a paleomonsoon proxy is supported by excellent overlap in $\delta^{18}O$ values of coeval stalagmites, and reveals a several stage evolution of the IASM. Monsoon activity strengthened in the early Holocene, consistent with other records from across the IPWP, suggesting that rising sea levels and flooding of the continental shelves produced a regional monsoon response. An observed in-phase (anti-phased) correlation with the Borneo (Flores) stalagmite record argues for a singular consistent driving mechanism over the last 9 ka and is attributed here to ENSO. Late Holocene weakening of the IASM 4.1–1.5 ka coincides with an increase in El Niño frequency and amplitude recorded in ENSO-sensitive proxies from across the Pacific and is consistent with Indo-Pacific and Australian pollen, charcoal, and lake level time series that indicate more extreme and variable drought conditions at this time. A 2‰ decrease in KNI-51 $\delta^{18}O$ values between 1.0 and 0.7 ka indicates a sharp rise in IASM strength, and represents the largest magnitude change in monsoon behavior of any interval during the Holocene. If ENSO is responsible for late Holocene IASM dynamics in the eastern Kimberley, then the

relationship between ENSO and the IASM in this region has weakened over the last millennium.

Acknowledgments

This research was funded by grants from the Kimberley Foundation (to KHW), and the National Science Foundation grant (AGS 1103413), the Center for Global and Regional Environmental Research, and Cornell College (to RFD). Samples obtained with the permission and understanding of the pastoral lease-holders and managers of Carlton Hill Station. We thank Donna Cavlovic for generous assistance in Kununurra, Tim Kelly in Mount Vernon, and an anonymous reviewer for insightful comments which improved this manuscript.

References

Alley, R.B., Mayewski, P.A., Sowers, T., Stuiver, M., Taylor, K.C., Clark, P.U., 1997. Holocene climate instability: a prominent, widespread event at 8200 yr ago. Geology 25, 483–486.
Arblaster, J.M., Meehl, G.A., Moore, A.M., 2002. Interdecadal modulation of Australian rainfall. Clim. Dyn. 18, 519–531.
Ashok, K., Behera, S.K., Rao, S.A., Weng, H., Yamagata, T., 2007. El Niño Modoki and its possible teleconnection. J. Geophys. Res.-ocean 112, C11007.
Asmussen, B., McInnes, P., 2013. Assessing the impact of mid-to-late Holocene ENSO-driven climate change on toxic Macrozamia seed use: a 5000 year record from eastern Australia. J. Archaeol. Sci. 40, 471–480.
Bar-Matthews, M., Matthews, A., Ayalon, A., 1991. Environmental controls on speleothem mineralogy in a karstic dolomitic terrain (Soreq Cave, Israel). J. Geol. 99, 189–207.
Bohm, F., Joachimski, M.M., Dyllo, W.-C., Eisenhauer, A., Lehnert, H., Reitner, J., Worheide, G., 2000. Oxygen isotope fractionation in marine aragonite of coralline sponges. Geochim. Cosmochim. Acta 64, 1695–1703.
Broadbridge, L.W., Hanstrum, B.N., 1998. The relationship between tropical cyclones near Western Australia and the Southern Oscillation Index. Aus. Meteor. Mag. 47, 183–190.
Broccoli, J.E., Dahl, K.A., Stouffer, R.J., 2006. Response of the ITCZ to Northern Hemisphere cooling. Geophys. Res. Lett. 33, L01702.
Cane, M.A., 2005. The evolution of El Nino, past and future. Earth Planet. Sci. Lett. 230, 227–240.
Chang, C.-P., Harr, P.A., McBride, J., Hsu, H.-H., 2004. Maritime continent monsoon; annual cycle and boreal winter variability. In: Chang, C.-P. (Ed.), East Asian Monsoon, World Scientific Series on Meteorology of East Asia, vol. 2. World Scientific Publishing Co. Pte. Ltd, Singapore, pp. 107–150.
Chang, C.-P., Wang, Z., Hendon, H., 2006. The Asian winter monsoon. In: Wang, B. (Ed.), The Asian Monsoon Praxis. Springer, Berlin, pp. 89–127.
Cheng, H., Edwards, R.L., Hoff, J., Gallup, C.D., Richards, D.A., Asmerom, Y., 2000. The half-lives of U-234 and Th-230. Chem. Geol. 169, 17–33.
Chiang, J.C.H., Bitz, C.M., 2005. Influence of high latitude ice cover on the marine intertropical convergence zone. Clim. Dyn. http://dx.doi.org/10.1007/s00382-005-0040-5.
Clement, et al., 2000. Suppression of El Niño during the mid-Holocene by changes in the Earth's orbit. Paleoceanography 15, 731.
Cobb, K.M., Adkins, J.F., Partin, J.W., Clark, B., 2007. Regional-scale climate influences on temporal variations of rainwater and cave dripwater oxygen isotopes in northern Borneo. Earth Planet. Sci. Lett. 264, 207–220.
Cobb, K.M., Westphal, N., Sayani, H.R., Watson, J.T., Di Lorenzo, E., Cheng, H., Edwards, R.L., Charles, C.D., 2013. Highly variabile El Niño -Southern oscillation throughout the Holocene. Science 339, 67–70.
Conroy, J.L., Overpeck, J.T., Cole, J.E., Shanahan, T.M., Steinitz-Kannan, M., 2008. Holocene changes in eastern tropical Pacific climate from a lake sediment record. Quat. Sci. Rev. 27, 1166–1180.
Cosford, J., Qing, H., Eglington, B., Mattey, D., Yuan, D., Zhang, M., Cheng, H., 2008. East Asian monsoon variability since the Mid-Holocene recorded in a high-resolution absolute-dated aragonite speleothem from eastern China. Earth Planet. Sci. Lett. 275, 296–307.
Craig, H., 1965. The measurement of oxygen isotope palaeotemperatures. In: Tongiorgi, E. (Ed.), Stable Isotopes in Oceanographic Studies and Palaeotemperatures. Consiglio Nazionale Della Richerche Laboratorio Di Geologia Nucleare, Pisa, pp. 161–182.
Dansgaard, W., 1964. Stable isotopes in precipitation. Tellus 16, 436–468.
de Choudens-Sánchez, V., González, L.A., 2009. Calcite and aragonite precipitation under controlled instantaneous supersaturation: elucidating the role of $CaCO_3$ saturation state and Mg/Ca ratio on calcium carbonate polymorphism. J. Sediment. Res. 79, 363–376.
Denniston, R.F., González, L.A., Asmerom, Y., Baker, R.G., Reagan, M.K., Bettis III, E.A., 1999. Evidence for increased cool season moisture during the middle Holocene. Geology 27, 815–818.
Denniston, R.F., Wyrwoll, K.-H., Asmerom, Y., Polyak, V.J., Humphreys, W., Cugley, J., Woods, D., Peota, J., Greaves, E., 2013. North Atlantic forcing of millennial-scale Australian monsoon variability during the Last Glacial. Quat. Sci. Rev. 72, 159–168.
Dorale, J.A., Liu, Z., 2009. Limitations of Hendy Test criteria in judging the paleoclimatic suitability of speleothems and the need for replication. J. Cave Karst Stud. 71, 73–80.
Gagan, M.K., Hendy, E.J., Haberle, S.G., Hantoro, W.S., 2004. Post-glacial evolution of the Indo-Pacific warm pool and El Niño–Southern oscillation. Quat. Int. 118–119, 127–143.
Genever, M., Grindrod, J., Barker, B., 2003. Holocene palynology of Whitehaven Swamp, Whitsunday Island, Queensland, and implications for the regional archaeological record. Palaeogeo. Palaeoclimatol. Palaeoecol. 201, 141–156.
Griffiths, M.L., Drysdale, R.N., Gagan, M.K., Zhao, J.X., Ayliffe, L.K., Hellstrom, J.C., Hantoro, W.S., Frisia, S., Feng, Y.X., Cartwright, I., Pierre, E.S., Fischer, M.J., Suwargadi, B.W., 2009. Increasing Australian-Indonesian monsoon rainfall linked to early Holocene sea-level rise. Nat. Geosci. 2, 636–639. http://dx.doi.org/10.1038/ngeo605.
Griffiths, M.L., Drysdale, R.N., Gagan, M.K., Zhao, J.-x., Ayliffe, L.K., Hellstrom, J.C., Hantoro, W.S., Frisia, S., Fen, Y.-x., Cartwright, I., St. Pierre, E., Fischer, M.J., Suwargdi, B.W., 2010. Evidence for Holocene changes in Australian-Indonesian monsoon rainfall from stalagmite trace elements and stable isotope ratios. Earth Planet. Sci. Lett. 292, 27–38.
Haberle, S.G., Ledru, M.-P., 2001. Correlations among charcoal records of fires from the past 16,000 years in Indonesia, Papua New Guinea, and Central and South America. Quat. Res. 55, 97–104.
Hendon, H.H., Lim, E.-P., Liu, G., 2012. The role of air-sea interaction for prediction of Australian summer monsoon rainfall. J. Clim. 25, 1278–1290.
Hendy, C., 1971. The isotopic geochemistry of speleothems – I. The calculation of the effects of different modes of formation on the isotopic composition of speleothems and their applicability as palaeoclimatic indicators. Geochim. Cosmochim. Acta. 35, 801–824.
Hiscock, P., Kershaw, A.P., 1992. Palaeoenvironments and prehistory of Australia's tropical Top End. In: Dodson, J. (Ed.), The Niave Lands:Prehistory and Environmental Change in Australia and the Southwest Pacific. Longman Cheshire, Melbourne, pp. 43–75.
Hong, C.-C., Li, T., 2009. The extreme cold anomaly over southeast Asia in February 2008: roles of ISO and ENSO. J. Clim. 22, 3787–3801.
IAEA/WMO: Global Network of Isotopes in Precipitation. The GNIP Database. http://isohis.iaea.org.
Jiang, H., Zipser, E.J., 2010. Contribution of tropical cyclones to the global precipitation from 8 seasons of TRMM data: regional, seasonal, and interannual variations. J. Clim. 23, 1526–1543.
Kiernan, K., 2004. Australia. In: Gunn, J. (Ed.), Encyclopedia of Caves and Karst Science. Taylor and Francis Publishers, New York, pp. 120–123.
Kim, S.-T., O'Neil, J.R., 1997. Equilibrium and nonequilibrium oxygen isotope effects in synthetic carbonates. Geochim. Cosmochim. Acta 61, 3461–3475.
Kim, S.-T., O'Neil, J.R., Hillaire-Marcel, C., Mucci, A., 2007. Oxygen isotope fractionation between synthetic aragonite and water: influence of temperature and Mg^{2+} concentration. Geochim. Cosmochim. Acta 71, 4704–4715.
Koutavas, A., Joanides, S., 2012. El Nino-Southern Oscillation extrema in the Holocene and Last Glacial Maximum. Paleoceanography 27, PA4208.
Koutavas, A., deMenocal, P.B., Olive, G.C., Lynch-Stieglitz, J., 2006. Mid-Holocene El Niño -Southern Oscillation (ENSO) attenuation revealed by individual foraminifera in eastern tropical Pacific sediments. Geology 34, 993–996.
Koutavas, A., Lynch-Stieglitz, J., Marchittom Jr., T.M., Sachs, J.P., 2002. El Niño-like pattern in ice age tropical Pacific sea surface temperature. Science 297, 226–230. http://dx.doi.org/10.1126/science.1072376.
Lachniet, M.S., Bernal, J.P., Asmerom, Y., Polyak, V., 2012. Uranium-loss and aragonite-calcite age discordance in a calcitized aragonite stalagmite. Quat. Geochronol. 14, 26–37.
Latif, M., Kleeman, R., Eckert, C., 1997. Greenhouse warming, decadal variability, or El Niño? an attempt to understand the anomalous 1990s. J. Clim. 10, 2221–2239.
Lécuyer, C., Hutzler, A., Amiot, R., Grosheny, D., Otero, O., Martineau, F., Fourel, F., Balter, V., Reynard, B., 2012. Carbon and oxygen isotope fractionations between aragonite and calcite of shells from modern molluscs. Chem. Geol. 332–333, 92–101.
Lewis, S.C., LeGrande, A.N., Kelley, M., Schmidt, G.A., 2010. Water vapour source impacts on oxygen isotope variability in tropical precipitation during Heinrich events. Clim. Past Discus. 6, 87–133.
Liu, Z., Otto-Bliesner, B., Kutzbach, J., Li, L., Shields, 2003. Coupled climate simulations of the evolution of global monsoons in the Holocene. J. Clim. 16, 2472–2490.
McBride, J.L., 1987. The Australian summer monsoon. In: Chang, C.P., Krishnamurti, T.N. (Eds.), Monsoon Meteorology. Oxford University Press, New York, pp. 203–231.
McBride, J.L., Nicholls, N., 1983. Seasonal relationships between Australian rainfall and the Southern Oscillation. Mon. Weather Rev. 111, 1998–2004.
McGlone, M.S., Kershaw, A.P., Markgraf, V., 1992. El Niño/Southern oscillation climatic variability in Australasian and south American palaeoenvironmental records. In: Diaz, H.F., Markgraf, V. (Eds.), El Niño: Historical and Palaeoclimatic Aspects of the Southern Oscillation. Cambridge University Press, pp. 435–462.
McGowan, H., Marx, S., Moss, P., Hammond, A., 2012. Evidence of ENSO mega-drought triggered collapse of prehistory Aboriginal society in northwest Australia. Geophys. Res. Lett. 39, L22702.
McGregor, H.V., Gagan, M.K., 2004. Western Pacific coral $\delta^{18}O$ records of anomalous Holocene variability in the El Niño-Southern Oscillation. Geophys. Res. Lett. 31, L11204.

Mickler, P.J., Banner, J.L., Stern, L., Asmerom, Y., Edwards, R.L., Ito, E., 2004. Stable isotope variations in modern tropical speleothems: evaluating equilibrium vs. kinetic isotope effects. Geochim. Cosmochim. Acta 68, 4381–4393.
Moise, A.F., Colman, R., 2009. Tropical Australia and the Australian Monsoon: general assessment and projected changes. In: Anderssen, R.S., Braddock, R.D., Newham, L.T.H. (Eds.), 18th World IMACS Congress and MODSIM09 International Congress on Modelling and Simulation, Modelling and Simulation Society of Australia and New Zealand and International Association for Mathematics and Computers in Simulation, July 2009, pp. 2042–2048.
Moy, C.M., Seltzer, G.O., Rodbell, D.T., Anderson, D.M., 2002. Variability of El Niño/Southern oscillation activity at millennial timescales during the Holocene epoch. Nature 420, 162–165.
Muller, J., McManus, J.F., Oppo, D.W., Francois, R., 2012. Strengthening of the northeast monsoon over the Flores sea, Indonesia, at the time of Heinrich event 1. Geology 40, 635–638.
Neale, Richard, Slingo, Julia, 2003. The Maritime continent and its role in the global climate: a GCM study. J. Clim. 16, 834–848. http://dx.doi.org/10.1175/1520-0442(2003)016<0834:TMCAIR>2.0.CO;2.
Newton, A., Thunell, R., Stott, L., 2006. Climate and hydrographic variability in the Indo-Pacific warm pool during the last millennium. Geophys. Res. Lett.s 33, L18710.
Nicholls, N., 1979. A possible method for predicting seasonal tropical cyclone activity in the Australian region. Mon. Weather Rev. 107, 1221–1224.
Nicholls, N., 1985. Predictability of interannual variations of Australian seasonal tropical cyclone activity. Mon. Weather Rev. 113, 1144–1149.
Nicholls, N., 1992. Recent performance of a method for forecasting Australian seasonal tropical cyclone activity. Aust. Meteorol. Mag. 40, 105–110.
Nicholls, N.N., Coauthors, 1996. Observed climate variability and change. In: Houghton, J.T., et al. (Eds.), Climate Change 1995. the Science of Climate Change. Cambridge University Press, pp. 135–192.
Nott, J., Price, D., 1994. Plunge pools and paleoprecipitation. Geology 22, 1047–1050.
Ortega, R., Maire, R., Deves, G., Quinif, Y., 2005. High-resolution mapping of uranium and other trace elements in recrystallized aragonite-calcite speleothems from caves in the Pyrenees (France): implication for U-series dating. Earth Planet. Sci. Lett. 237, 911–923.
Partin, J.W., Cobb, K.M., Adkins, J.F., Clark, B., Fernandez, D.P., 2007. Millennial-scale trends in West Pacific warm pool hydrology since the last glacial maximum. Nature 449, 452–455. http://dx.doi.org/10.1038/nature06164.
Power, S., Casey, T., Folland, C., Colman, A., Mehta, C., 1999. Inter-decadal modulation of the impact of ENSO on Australia. Clim. Dyn. 15, 319–324.
Railsback, L.B., Fleisher, C.J., Brook, G.A., Jian, C., Kalin, R., 1994. Environmental controls on the petrology of a late Holocene speleothem from Botswana with annual layers of aragonite and calcite. J. Sediment. Res. 64, 147–155.
Revell, C.G., Goulter, S.W., 1986. South Pacific tropical cyclones and the Southern oscillation. Mon. Weather Rev. 114, 1138–1145.
Rowe, C., 2007. A palynological investigation of Holocene vegetation change in Torres straight, seasonal tropics of northern Australia. Palaeogeogr. Palaeoclimatol. Palaeoecol. 251, 830103.
Sachs, J.P., Sachse, D., Smittenberg, R.H., Zhang, Z., Battisti, D.S., Golubic, S., 2009. Southward movement of the Pacific intertropical convergence zone AD 1400–1850. Nat. Geosci. 2, 519–525.
Saji, N.H., Goswami, B.N., Vinayachandran, P.N., Yamagata, T., 1999. A dipole mode in the tropical Indian Ocean. Nature 401, 360–363.
Shulmeister, 1999. A Holocene pollen record from lowland tropical Australia. Holocene 2, 107.
Shulmeister, Lees, 1995. Pollen evidence from tropical Australia of an ENSO-dominated climate at c. 4000 BP. Holocene 5, 10.
Slingo, J.M., 1998. Extratropical forcing of tropical convection in a northern winter simulation with the UGAMP GCM. Q. J. R. Meteorol. Soc. 124, 27–51.
Stott, L., Poulsen, C., Lund, S., Thunell, R., 2002. Super ENSO and global climate oscillations at millennial time scales. Science 297, 222–226. http://dx.doi.org/10.1126/science.1071627.
Suppiah, R., 1992. The Australian summer monsoon: a review. Prog. Phys. Geogr. 16, 283–318.
Suppiah, R., Wu, X., 1998. Surges, cross-equatorial flows and their links with the Australian summer monsoon circulation and rainfall. Aust. Meteorol. Mag. 47, 113–130.
Tarutani, T., Clayton, R.N., Mayeda, T.K., 1969. Effect of polymorphism and magnesium substitution on oxygen isotope fractionation between calcium carbonate and water. Geochim. Cosmochim. Acta 33, 987–996.
Taschetto, A.S., England, M.H., 2009. An analysis of late twentieth century trends in Australian rainfall. Int. J. Clim. 29, 791–807.
Taschetto, et al., 2011. The contribution of Indian ocean sea surface temperature anomalies on Australian summer rainfall during El Niño events. J. Clim. 24, 3734–3747.
Tierney, J.E., Oppo, D.W., LeGrande, A.N., Huang, Y., Rosenthal, Y., Linsley, B.K., 2012. The influence of Indian Ocean atmospheric circulation on warm pool hydroclimate during the Holocene epoch. J. Geophys. Res. 117, D19108.
Walliser, D.E., Gautier, C., 1993. A satellite-derived climatology of the ITCZ. J. Clim. 6, 2162–2174.
Wang, Y.J., Cheng, H., Edwards, R.L., An, Z.S., Wu, J.Y., Shen, C.C., Dorale, J.A., 2001. A high-resolution absolute-dated late Pleistocene monsoon record from Hulu Cave, China. Science 294, 2345–2348. http://dx.doi.org/10.1126/science.1064618.
Wang, Y.J., Cheng, H., Edwards, R.L., He, Y.Q., Kong, X.G., An, Z.S., Wu, J.Y., Kelly, M.J., Dykoski, C.A., Li, X.D., 2005. The Holocene Asian monsoon: links to solar changes and North Atlantic climate. Science 308, 854–857.
Wang, L., Kodera, K., Chen, W., 2012. Observed triggering of tropical convection by a cold surge: implications for MJO initiation. Quat. J. R. Meteor. Soc. 138, 1740–1750. http://dx.doi.org/10.1002/qj.1905.
Webster, P.J., Palmer, T.N., 1997. The past and future of El Nino. Nature 390, 562–564.
Wheeler, M.C., Hendon, H.H., Cleland, S., Meinke, H., Donald, A., 2009. Impacts of the Madden–Julian oscillation on Australian rainfall and circulation. J. Clim. 22, 1482–1498.
Wheeler, M.C., McBride, J.L., 2011. Australasian monsoon. In: Lau, W.K.M., Waliser, D.E. (Eds.), Intraseasonal Variability in the Atmosphere-ocean Climate System, second ed. Springer, pp. 147–198.
Wu, Renguang, Kirtman, Ben P., 2007. Roles of the Indian ocean in the Australian summer monsoon–ENSO relationship. J. Clim. 20, 4768–4788.
Wyrwoll, K.H., Hopwood, J., Mckenzie, N.L., 1992. The Holocene paleohydrology and climatic history of the northern Great Sandy Desert – Fitzroy trough: with special reference to the history of the Northwest Australian Monsoon. Clim. Change 22, 47–65.
Wyrwoll, K.-H., Liu, Z., Guangshan, C., Kutzbach, J.E., Liu, X., 2007. Sensitivity of the Australian summer monsoon to tilt and precession forcing. Quat. Sci. Rev. 26, 3043–3057.
Yeh, S.W., Kug, J.S., Dewitte, B., Min-Ho Kwon, M.H., Kirtman, B.P., Jin, F.F., 2009. El Niño in a changing climate. Nature 461, 511–514.